NASA TECHNICAL MEMORANDUM 107755

THE GROWTH OF SMALL CORROSION FATIGUE CRACKS IN ALLOY 2024

R. S. Piascik and S. A. Willard

APRIL 1993

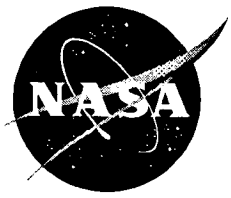

National Aeronautics and
Space Administration

Langley Research Center
Hampton, Virginia 23681-0001

THE GROWTH OF SMALL CORROSION FATIGUE CRACKS IN ALLOY 2024

Robert S. Piascik[1] and Scott A. Willard[2]

[1]Mechanics of Materials Branch
[2]Lockheed Engineering & Sciences Company
NASA-Langley Research Center
Hampton, VA 23681-0001

Abstract

The corrosion fatigue crack growth characteristics of small surface and corner cracks in aluminum alloy 2024 is established. The damaging effect of salt water on the early stages of small crack growth is characterized by: 1. crack initiation at constituent particle pits, 2. intergranular microcracking for $a \leq 100$ μm, and 3. transgranular small crack growth for $a \geq 100$ μm. In aqueous 1% NaCl and at a constant anodic potential of -700 mV_{SCE}, small cracks exhibit a factor of three increase in fatigue crack growth rates compared to laboratory air. Small cracks exhibit accelerated corrosion fatigue crack growth rates at low levels of ΔK (< 1 $MPa\sqrt{m}$) below long crack ΔK_{th}. When exposed to Paris regime levels of crack tip stress intensity, small corrosion fatigue cracks exhibit growth rates similar to that observed for long cracks. Results suggest that crack closure effects influence the corrosion fatigue crack growth rates of small cracks ($a \geq 100$ μm). This is evidenced by similar small and long crack growth behavior at various levels of R. Contrary to the corrosion fatigue characteristics of small cracks in high strength steels, no pronounced chemical crack length effect is observed for alloy 2024 exposed to salt water.

I. Introduction

The growth kinetics of small fatigue cracks are of critical importance to material durability. Research has shown that the propagation of small cracks from surface defects (5 μm to 10 μm) constitute a large percentage (50% to 90%) of the total fatigue life of metallic components.[(1)] Thus, errors in the prediction of small crack da/dN can result in erroneous damage tolerant based life prediction.

A problem arises because small cracks propagate at unpredictably accelerated rates compared to long fatigue cracks.[(2,3)] The difference in long and small crack behavior is

attributed to (1) diminished crack tip shielding (closure) effects at small crack sizes and/or (2) possible violation of plasticity and continuum mechanics assumptions associated with the use of linear elastic crack tip stress intensity factor range (ΔK) for microstructurally small cracks. Compounding the small crack problem are complex environmental effects. Corrosion fatigue research of high strength steels in salt water has shown that chemically-short[1] cracks (<5 mm) propagate 1.5 to 500 times faster than long cracks subjected to the same mechanical driving force.[4,5] For steels in salt water (aqueous NaCl), accelerated small crack growth rate is attributed to reduced corrosion product and wake-roughness induced closure, increased concentration of crack tip reactants which depend on occluded crack geometry and possibly hydrogen enhanced crack tip plasticity.[6-8]

Small crack effects during corrosion fatigue have not been reported for nonferrous alloys. Limited research for high strength aluminum alloys exposed to salt water, suggest little chemical-crack-length effect for short through thickness cracks.[9,10] The objective of the current study is to extend the chemical crack size data base for aluminum alloys. Here, corrosion fatigue research is conducted to study the effect of deaerated aqueous NaCl on the fatigue crack growth behavior of naturally nucleated surface and corner cracks, sized between 100 μm and 1.5 mm.

II. Experimental Procedure

Constant load amplitude fatigue crack growth experiments were conducted on pin loaded, blunt notched, extended compact tension (ECT) specimen shown in Figure 1a. All tests were conducted using a commercially available Al-Cu-Mg alloy 2024-T3 sheet, 2.0 mm thick. The growth of small surface cracks located at the root of the polished (through 0.3 μm diamond paste) blunt notch were monitored *in situ* by using a long focal length (15 cm to 38 cm) microscope. Surface crack length measurements were performed at a magnification of 500X with a resolution of approximately 1 μm (in air) and 3 μm (in salt water). All crack length measurements were performed while the specimen remained at 70% of maximum load. Small

---

[1] The term "chemically-small cracks" refers to the phenomenon where crack tip chemical driving force is crack size dependent and accelerated small corrosion fatigue crack growth rates are not predicted by long corrosion fatigue crack growth characteristics.

surface and corner crack growth rates and stress intensity factors were calculated assuming uniform semicircular (a/c=1, where a and c are defined in Figure 1b) crack geometry and procedures documented elsewhere.[1,11-14] The stress intensity factor (K) solution for small cracks in the ECT specimen is defined in Appendix A.

Microscope and replica based small crack growth experiments in air were conducted at constant ΔP (R=0.05) for $a \geq 35$ μm and $a \geq 10$ μm, respectively. Corrosion fatigue crack growth testing was conducted at high and low R by varying P_{min} at constant P_{max}. Here, reduced *in situ* crack length measurement resolution limited the study of corrosion fatigue cracks to $a \geq 100$ μm and to high R ($0.7 \leq R \leq 0.8$) testing for the investigation of low ΔK growth rates.

The direct current electrical potential drop method was used to monitor the growth of through thickness cracks. Refer to Appendix B for the through thickness crack K solution for the ECT specimen. Long crack computer-controlled experiments were conducted by continuously adjusting the load to maintain the programmed ΔK and stress ratio (R). Two decreasing ΔK methods were used; (1) constant R (0.05) and (2) variable R ($0.2 \leq R \leq 0.9$) at constant K_{MAX} (15 MPa$\sqrt{m}$).[15,16]

A 1.5 liter O-ring sealed plastic chamber was used for salt water corrosion fatigue experiments. The mid-half of the ECT specimen was continuously immersed in helium deaerated 1% NaCl (pH = 8). All aqueous NaCl experiments were conducted under constant electrode potential using a potentiostat, two fully immersed platinum counter electrodes and a Ag/AgCl reference electrode. The distilled water/salt solution was continuously circulated through the test chamber at a rate of 30 ml/min. from a reservoir containing 25 L of argon deaerated NaCl solution. A quartz window located on the side of the chamber and adjacent to the notch was used for *in situ* long focal length microscope viewing of the notch root surface fatigue cracks.

Potentiodynamic testing of alloy 2024-T3 in 1% NaCl revealed an open circuit potential of -600 mV_{SCE} and -1090 mV_{SCE} for 1% NaCl air saturated and an helium deaerated solution, respectively.[2] Based on a breakaway (pitting) potential of approximately -600 mV_{SCE} for both aerated and deaerated solutions, all deaerated corrosion fatigue experiments were conducted at

---

[2] All electrode potentials are stated with respect to the saturated calomel electrode (SCE).

a constant electrochemical potential of -700 mV_{SCE}.

III. Results

A. Blunt Notch Small Crack da/dN Experiments

Small fatigue crack growth experiments were conducted in air using the blunt notch ECT specimen. The purpose of these experiments was to compare small crack growth rates determined by the long focal length microscope measurement technique with rates determined by the standard acetate replica technique[13]. Figure 2 represents the fatigue crack growth characteristics of surface and corner cracks of lengths ranging from 10 μm to 1000 μm for replica based measurements and 35 $\mu m \leq a \leq 1400$ μm for microscope based measurements. When multiple cracks were observed, special care was taken during data analysis to eliminate data for crack configurations where possible interaction effects could influence crack tip ΔK.[11] Typical of small cracks, the growth rate data shown in Figure 2 are variable and presumed to be a result of crack front/microstructure interaction.[17] A power law fit of the microscope and replica data, dashed and solid lines in Figure 2, respectively, show that both measurement techniques yield similar small crack growth behavior for alloy 2024. Further comparisons with literature data for similar R show that the extended compact tension results correlate well with replica based small crack growth data generated from the single edge notch specimen.[11] It should be noted that these data suggest that the presence of acetone on the notch surface during replication does not alter 2024 fatigue crack growth rates.[13]

B. Comparison of Small Crack da/dN in Salt Water and Air

The results in Figure 3 show that small surface cracks ranging in size from 100 μm to 1400 μm exhibit accelerated fatigue crack growth rates in deaerated 1% NaCl (-700 mV_{SCE}) compared to laboratory air. The solid line in Figure 3 is a power law fit of the microscope based salt water data at variable R. The dashed lines represent power law fits for fixed R microscope and replica based air data; the R=0.05 line is from Figure 2 and R=0.5 is by others[11]. Similar fatigue crack growth behavior is shown in air for R of 0.05 and 0.5. These results suggest that small cracks exhibit reduced R dependence and therefore a single curve fit of variable R data, used here for salt water, approximates small crack da/dN versus ΔK

corrosion fatigue behavior. A comparison of the power law fit for salt water and air data show that high ΔK (low R) da/dN are accelerated by a factor of 3 in salt water. At low ΔK and high R, aqueous NaCl crack growth rates exhibit a similar 3 fold increase compared to air rates. The limited small crack data shown in Figure 3 show that accelerated corrosion fatigue crack growth rates are observed at low ΔK (< 1 MPa$\sqrt{m}$). It should be noted that the observed scatter in corrosion fatigue crack growth rates is characteristic of the small crack propagation.[2,3] Individual cracks can grow considerably faster or slower than the general trends noted by the power law curve fit shown in Figure 3.

C. Comparison of Small and Long Crack da/dN in Salt Water

The corrosion FCP behavior of surface and corner cracks, sized from 100 μm to 1400 μm, is compared to long through thickness cracks, 14 mm to 28 mm in length in Figure 4. Long and small crack growth experiments were conducted under identical potenstiostat controlled salt water environment. For $\Delta K > 2.5$ MPa$\sqrt{m}$ and low R (0.05), long crack growth rates are in general comparable to the power law fit of the small crack data. The slightly higher long crack growth rates observed for $\Delta K > 5$ MPa$\sqrt{m}$ is consistent with results obtained for air data.[18] Small differences in long and small crack growth rates (da/dN and dc/dN, respectively) for $\Delta K \geq 5$ MPa$\sqrt{m}$ may be linked to material anisotropy. Researchers have suggested that cracking in a and c directions, defined in Figure 1b, are influenced by differences in the orientation of microstructural barriers, i.e. grain boundaries, relative to the crack path.[18] The constant K_{max}/variable R results shown in Figure 4 exhibit similar trends compared to that observed in air by Herman et.al.[15]; i.e., the elevated mean stress FCG data track the upper bound of small crack corrosion fatigue results. At low ΔK and high R, similitude is no longer maintained; long cracks develop a fatigue crack growth threshold and small cracks exhibit accelerated corrosion fatigue crack growth rates for $\Delta K < 1$ MPa$\sqrt{m}$.

D. Fractography of Initiation and Growth of Small Cracks

After corrosion fatigue testing, detailed fractography was performed to characterize the effect of salt water environment on the initiation and growth of small cracks in alloy 2024.

1. Initial Stages of Crack Growth: Figure 5 is a montage showing a portion of the

blunt notch specimen (insert) pulled to failure by overload after corrosion fatigue (CF) testing in 1% NaCl (-700 mV_{SCE}). Two prominent corrosion fatigue cracks were monitored by the long focal length microscope during the CF test. Located at the top of Figure 5 is the overload fracture surface containing one of the main fatigue cracks (not readily visible). The second corrosion fatigue crack located below the main fracture surface (A in Figure 5) is detailed at higher magnification in Figure 6. Here, the crack has been fully opened by the overload. During the overload, the blunt notch region was purposely strained, as noted by the deformed side surfaces in Figure 5. This process opened the tightly closed corroded areas on the notch surface, making them readily visible at low magnification.

Figure 7a reveals the extensive pitting on the notch surface (C in Figure 5). Figure 7b shows higher magnification views of pits at location X, Y and Z in Figure 7a. Emission dispersive X-ray analysis (EDX), Figure 8, of these regions show that pitting occurs at Fe and Si rich surface constituent particles. Regions exhibiting no pitting revealed no evidence of Fe and Si, insert in Figure 8. Detailed examination of the notch surface shown in Figure 5 revealed that pits located in the region of highest stress exhibit the greatest propensity for microcracking. The vast majority of microcracks are oriented nearly normal to the applied load, further suggesting that such cracking is stress related. Regions of low stress, farther down on the notch surface and away from the notch root, contain pitting with no evidence of cracking. Figure 9 shows a 100 μm surface crack located in the high stress region that was opened by the overload. The exposed inner surfaces of this crack exhibits a rock candy morphology, characteristic of intergranular (IG) cracking. Assuming a semicircular shaped crack front, intergranular penetration may extend 50 μm into the material.

Metallographic sectioning of the blunt notch region, Figure 10, confirmed that the initial stage of cracking is associated with a stress assisted intergranular cracking process.[18] Careful examination of the microstructural crack path was performed by repeated metallographic sectioning followed by polishing and a Keller's etch. Metallographic examinations of the sectioned, polished and etched surfaces confirmed intergranular (IG) microcracking in the high stress region and no IG cracking in the low stress region of the blunt notch. Figure 11 is a high magnification view of region D in Figure 10 showing intergranular cracking to a depth of 60 μm. Further examination of the high stress region revealed that IG microcracks extend up to

100 μm into the material.

2. Crack Propagation: Figure 12 is a series of SEM micrograph at different magnification showing the region of crack initiation and the typical fracture morphology of a semicircular shaped corrosion fatigue surface crack (a=315 μm) that was exposed to deaearated NaCl (-700 mV_{SCE}). The fatigue crack initiated at the constituent particle pit shown in Figure 12b and marked by large arrows in Figures 12a and 12c. The crack is located mid-thickness in the high stress region of the notch root surface. Following initiation and IG microcracking, the crack grew primarily along a crystallographic (transgranular) crack path. During growth, the crack front maintained a nearly semicircular shape as shown by the intermediate crack arrest mark noted by the dashed line in Figure 12a. The dark region, marked by the dashed line in Figure 12a and shown in greater detail in Figure 12c, exhibits severe corrosion that occurred during crack arrest. The fracture surface region adjacent to the heavily pitted dark region contains secondary cracks marked by small arrows in Figure 12c. This is evidence of stress assisted intergranular cracking that occurred during crack arrest. Further cyclic loading reestablished transgranular fatigue crack growth. Examination of other corrosion fatigue cracks reveal no evidence of crack arrest suggesting that in many instances microstructural barriers did not restrain crack propagation.

Shown in Figure 13a are two corner cracks, A and B, that grew concurrently during corrosion fatigue testing. *In situ* long focal microscope observations showed that both corner cracks initiated at constituent particle pits located in the high stress region and near the edge of the blunt notch surface (marked by the large arrows in Figure 13a). Both cracks rapidly evolved into corner cracks that grew with quartercircular shaped crack fronts. Little evidence of intergranular cracking is observed at the site of crack initiation. Crack B does exhibit intergranular cracking at the point marked by the arrow in Figure 13b. Here, corner crack B coalesced with a small (50 μm) surface IG crack similar to the small intergranular incipient surface cracks marked by small arrows in Figure 13a. The small region of IG cracking noted in Figure 13b exhibits a surface free of thick corrosion products, suggesting that crack coalescence occurred during the final stages of the experiment and IG microcracks are some what closed, not allowing excessive communication with the bulk environment.

IV. Discussion

The early stages of corrosion fatigue cracking in alloy 2024 is characterized by three distinct processes illustrated in Figure 14. Corrosion fatigue crack initiation occurs within highly localized regions associated with surface constituent particle pitting. The early stage of crack growth, "microcracking", proceeds by a stress assisted intergranular cracking process. The third stage of small corrosion fatigue crack propagation is characterized by transgranular growth. Each of these phenomena (pitting, intergranular crack and transgranular corrosion FCP) have been well characterized by previous research, but little is known about these damage processes as they relate to the growth of small corrosion fatigue cracks.

A. Stage 1 - Pitting

Detailed microscopy and emission dispersive X-ray analysis results shown in Figures 7 and 8 reveal that constituent particles (Fe-Cu-Si rich phase) pitting are sites for corrosion fatigue crack initiation. The microsegragation of Cu and Fe in the form of Cu-Fe rich constituent particles (Si has little effect on pitting corrosion behavior) and Cu rich boundary phases render aluminum alloy 2024 more susceptible to pitting and intergranular corrosion. These phases form small cathodes embedded in a large anode matrix which result in accelerated localized corrosion.[20-24] Pits form rapidly when the anodic region surrounding the surface constituent phase, region Y in Figure 7b, is preferentially attacked. Intergranular microcracks nucleate at these regions of high stress concentration and grow by a process of linking neighboring microcracks as illustrated by regions X and Z in Figure 7b. Presumably, an aggressive occluded cell (pit) environment is formed by the depletion of dissolved oxygen, accumulation of metal cations and chloride ion, and increased metal ion hydrolysis resulting in lower pH.[19,24] These processes serve to increase local dissolution rates which influence the growth mechanism of the emerging microcracks.

B. Stage 2 - Microcracking

The early stage of corrosion fatigue crack growth is characterized by an intergranular cracking process as seen in Figures 9 and 10. Intergranular microcracks are typically less than

100 μm in depth and found only in regions where the combination of high stress and occluded pitting chemistry occur. These observations are consistent with those of Ketcham, where the combination of stress and low pH are required to provide the environment necessary to produce intergranular cracking in rapidly quenched[3] Al-Cu-Mg alloy exposed to salt water solution.[19]

Limited testing show that cyclic stress accelerates the initiation of intergranular microcracking. Seven day static and cyclic load experiments were conducted under identical environmental conditions, 1% NaCl (pH = 8) and constant electrochemical potential of -700 mV_{SCE}. Three different loading schemes were used; static loading P_{static}=350 lb., ripple loading P_{max}=350 lb. (R=0.8), and high cyclic loading P_{max}=350 lb. (R=0.2). Detailed SEM examination of the blunt notch surface revealed that only the high cyclic loading conditions promoted intergranular cracking. These limited results suggest that increased cyclic strain exacerbates pit initiated intergranular microcracking in alloy 2024. The synergistic effect of cyclic loading in combination with constituent particle pit environment are consistent with a film rupture damage mechanism.[26,27] Presumably, increased damage produced by cyclic strain results in a critical dislocation structure. Dislocation slip steps penetrate the occluded cell passive oxide surface layer continuously exposing an anodic path for grain boundary microcracking. The initiation of microcracking is controlled by the repassivation kinetics of the pit walls and the applied strain range.[28] The fatigue crack growth kinetics of pit initiated microcracks is unknown. In many cases, a web of tight microcracks radiate from pits, forming a complex geometry of crack interactions.

The transition from intergranular microcracks to transgranular cracking depicted in Figure 14 suggests a change in the crack growth damage process. Presumably, a critical crack depth is achieved where the crack front environment is no longer influenced by the constituent particle occluded cell chemistry. This transition process is suggested based on detailed examinations of long crack corrosion fatigue surfaces where local regions of intergranular cracking are observed only at low ΔK. At high ΔK, the fast moving crack front rapidly passes

---

[3] The phenomenon of intergranular cracking is well documented for Al-Cu-X systems; the Cu rich phases that precipitate at boundaries create an anodic path for intergranular cracking.[19,24,25] Typically, susceptibility to intergranular corrosion is linked to slow quenching rates following solution heat treatment of a naturally aged Al-Cu-Mg alloy. It is important to note that Ketchem's work suggests that under stress and low pH salt water environment IGA can occur in "nonsusceptible" Al-Cu-Mg alloys.[19]

intersecting constituent particles and an IG cracking environment is not formed.

C. Stage 3 - Small Crack Propagation

The damaging effect of salt water on small transgranular surface and corner cracks is characterized by a factor of three increase in rates compared to laboratory air. Crack closure effects are likely for crack depths greater than 100 μm since similar long crack Paris regime rates are observed and elevated mean stress (constant K_{max}) long crack growth rates bound most small crack growth data. Similar corrosion fatigue crack growth behavior for small surface cracks and long through thickness cracks suggest that chemical crack length effects are not dominant and no appreciable chemical-crack-geometry effect is operative.[4-8]

A lack of small/long crack growth similitude is observed for $\Delta K \leq 1$ MPa$\sqrt{m}$. Here, small corrosion fatigue cracks ($a=100\mu m$) exhibit accelerated high R da/dN compared to long through thickness corrosion fatigue cracks. These 100 μm cracks are large compared to microstructure; multiple grains, 5 or more, intersect the semicircular crack fronts, suggesting that the continuum argument and LEFM are reasonable. Accelerated small crack corrosion FCG rates suggests that increased crack tip driving force is related to reduced crack closure effects and/or enhanced transport of deleterious species to the crack tip.

IV. Summary and Conclusions

The previously unknown corrosion fatigue crack growth characteristics of small surface and corner cracks are established for alloy 2024. Results show that no dominant chemical crack length effect is present and conventional long through thickness crack growth testing at high R conservatively simulates the Paris regime response of small cracks (150 $\mu m \leq a \leq 1400$ μm) in salt water. For ΔK less than long crack threshold, small surface and corner cracks (100 $\mu m \leq a \leq 150$ μm) exhibit accelerated corrosion fatigue crack growth rates compared to long through thickness cracks; here, similitude is not maintained.

The following specific conclusions are drawn based on the small corrosion fatigue crack growth data for alloy 2024.

1. The growth of small corrosion fatigue cracks in alloy 2024 is characterized by a distinct sequence of processes. Crack initiation occurs at constituent particle pits followed by

intergranular microcracking that transitions to a transgranular fracture mode at a depth of approximately 100 μm.

2. Intergranular microcracking is exacerbated by high cyclic stress and occluded pit chemistry. The transition from IG cracking to transgranular corrosion fatigue crack growth is linked to a critical crack depth where the crack front environment is no longer influenced by the constituent phase local chemistry.
3. No chemical crack length effects are observed. In potenstiostatically controlled salt water environment, small surface and corner cracks of depths ranging from 100 μm to 1.4 mm exhibit similar low R Paris regime fatigue crack growth characteristics compared to long through thickness cracks (14 mm $\leq$ a $\leq$ 27 mm).
4. Small crack corrosion fatigue crack growth rates in salt water are accelerated by a factor of 3 compared to fatigue crack growth rates air.

APPENDIX A

Blunt Notch Surface and Corner Crack Stress-Intensity Factor Equations

The crack tip stress intensity factor (K) solution for the ECT specimen was obtained by equating local notch root stresses (σ) for the single edge notch (SENT)[14] and the ECT specimens, i.e.,

$$\sigma_{SENT} = \sigma_{ECT} \tag{1}$$

The SENT specimen stress intensity factor equation is given by:

$$K_{SENT} = S(\pi a/Q)^{1/2}(F_{jn}) = (\sigma_{SENT}/K_T)(\pi a/Q)^{1/2}(F_{jn}) \tag{2}$$

where:

K_{SENT} and K_{ECT} =stress intensity factor for SENT and ECT specimens, respectively.
S = SENT remote stress = σ_{SENT}/K_T.
K_T = notch stress concentration factor.
a = surface and corner crack dimensions defined in Figure 1b.
Q = shape factor; same for SENT and ECT.
F_{jn} = boundary correction factor; same for SENT and ECT = f(a/c,a/t,c/r,c/W,r/t,r/W,Q), where: Θ = angle at which K is determined ($-\pi/2 \leq \Theta \leq \pi/2$), other parameters are defined in Figure 1.

The same form of the equation can be applied to the ECT specimen for crack depth, c < t (defined in Figure 1b), as shown by equation 3.

$$K_{ECT} = (\sigma_{ECT}/K_T)(\pi a/Q)^{1/2}(F_{jn}) \quad (3)$$

The boundary force method[29] was used to obtain the local stress state at the notch root for the ECT specimen and is given by

$$\sigma_{ECT} = 18.4(P/WB) \quad (4)$$

where:

P = load

W and B are defined in Figure 1

Substituting equation 4 into equation 3 yields the following expression for K_{ECT}.

$$K_{ECT} = (18.4/K_T)(P/WB)(\pi a/Q)^{1/2}(F_{jn}) \quad (5)$$

The final expression for K_{ECT} is obtained by substituting in the K_T value of 3.17 for the SENT specimen.

$$K_{ECT} = 5.8(P/WB)(\pi a/Q)^{1/2}(F_{jn}) \quad (6)$$

APPENDIX B

Stress-Intensity Factor Equation for Blunt Notch ECT Through Thickness Crack

The stress intensity factors for a through thickness crack emanating from a semi-circular notch subjected to remote pin loading is

$$K = (P/WB)(\pi c)^{1/2}F_m \quad (7)$$

for $d/W \leq c/W \leq 0.8$. The boundary correction factor F_m is

$$F_m = F_n F_w \quad (8)$$

The function F_n is given by

$$F_n = 0.9 + 3.0\tau - 2.42\tau^2 + 2.46\tau^3 + 1.37\tau^4 \quad (9)$$

where:

$\tau = 1/(1+c/r)$

and the function F_w is given by

$$F_w = 3.13 + 2.43\gamma - 48.28\gamma^2 + 281.84\gamma^3 - 537.89\gamma^4 + 372.32\gamma^5 \quad (10)$$

where:

$\gamma = (c+d)/W$

Acknowledgements

Mr. W.T. Howard assisted with corrosion fatigue methodology development and testing. Dr. J.C. Newman provided the stress analysis and stress intensity factor solution for the extended compact blunt notch specimen. Metallography, EDX analysis and potentiodynamic polarization data were provided by Mr. P.N. Kalil, Mr. R.A. Edahl, Jr. and Dr. A.C. Van Orden, respectively. These important contributions are gratefully acknowledged.

References

1. J.C. Newman, Jr., E.P. Phillips, M.H. Swain and R.A. Everett, Jr., in Advances in Fatigue Lifetimes Predictive Techniques, ASTM STP 1122, M.R. Mitchell and R.W. Landgraf, eds., ASTM, Philadelphia, PA, pp. 5-27 (1992).

2. Small Fatigue Cracks, R.O. Ritchie and J. Lankford, eds., TMS-AIME, Warrendale, PA (1986).

3. The Behavior of Short Fatigue Cracks, K.J. Miller and E.R. de los Rios, eds., Mechanical Engineering Publications Limited, London, UK (1986).

4. R.P. Gangloff and R.P. Wei, in Small Fatigue Cracks, R.O. Ritchie and Lankford, eds., TMS-AIME, Warrendale, PA. pp. 239-264, (1986).

5. R.P. Gangloff and D.J. Duquette, in Chemistry and Physics of Fracture, R.M. Latanision and R.H. Jones, eds., Martinus Nijhoff Publishers BV, Netherlands p. 612 (1987).

6. A. Turnbull, Matls. Sci. Tech., Vol. 1, pp. 700-710 (1985).

7. A. Turnbull and D.H. Ferris, in Corrosion Chemistry Within Pits, Crevices and Cracks, A. Turnbull, ed., HMSO, London, UK, pp. 397-412 (1984).

8. R.P. Wei and R.P. Gangloff, in Environmentally Assisted Crack Growth in Structural Alloys: Perspectives and New Directions, STP 1020, R.P. Wei and R.P. Gangloff, eds., ASTM, Philadelphia, PA, pp. 233-264 (1989).

9. R.S. Piascik and R.P. Gangloff, Metall. Trans. A, Vol. 22A, pp. 2415-2428 (1991).

10. R.S. Piascik, "Mechanisms of Intrinsic Damage Localization During Corrosion Fatigue: Al-Li-Cu System", PhD Dissertation, University of Virginia, Charlottesville, VA (1989).

11. J.C. Newman, Jr. and P.R. Edwards, Short-Crack Growth Behavior in an Aluminum Alloy - An AGARD Cooperative Test Programme, AGARD 732 (1988).

12. J.C. Newman, Jr., M.H. Swain, and E.P. Phillips, in Small Fatigue Cracks, R.O. Ritchie and J. Lankford, eds., TMS-AIME, Warrendale, PA, pp. 427-452 (1986).

13. M.H. Swain, in Small Crack Test Methods, ASTM STP 1149, J. Larsen and J. Allison, eds., ASTM, Philadelphia, PA, pp. 34-56 (1992).

14. J.C. Newman, Jr., in Small Crack Test Methods, ASTM STP 1149, J. Larsen and J.E. Allison, eds., ASTM, Philadelphia, PA, pp. 6-33 (1992).

15. W.A. Herman, R.W. Hertzberg and R. Jaccard, Fat. Engr. Matls. and Structures, Vol.11, pp. 303-320 (1988).

16. W.A. Herman, R.W. Hertzberg, C.H. Newman and R Jaccard, in Fatigue 87, R.O. Ritchie and E.A. Starke, Jr., eds., EMAS, West Midlands, UK, pp. 819-828 (1987).

17. J. Lankford and D.L. Davidson, in Small Fatigue Cracks, R.O. Ritchie and J. Lankford, eds., TMS-AIME, Warrendale, PA, pp. 51-71 (1986).

18. J.C. Newman, Jr., X.R. Wu, S.L. Venneri and C.G. Li, A Fatigue and Fracture Mechanics Cooperative Program on Small Crack Effects in High-Strength Aluminum Alloys, NASA RP Report to be published, NASA Langley Reseach Center, Hampton, VA, To be published as a NASA RP (1993).

19. S.J. Ketcham, Corrosion Science, Vol.7, pp. 305-314 (1967).

20. J.R. Gavele and S.M. DeMicheli, Corrosion Science, Vol. 10, pp. 795-802 (1970).

21. S.J. Ketcham and F.H. Haynie, Corrosion, Vol. 19, pp. 242-247 (1963).

22. H. Kaesche, in Localized Corrosion, R.W Staehle, B.F. Brown, J. Kruger, and A. Agrawal, eds., NACE, Houston, TX, pp. 516-525 (1971).

23. G.C. Wood, W.H. Sutton, J.A. Richardson, T.N.K. Riley and A.G. Malherbe, in Localized Corrosion, R.W Staehle, B.F. Brown, J. Kruger, and A. Agrawal, eds., NACE, Houston, TX, pp. 526-539 (1971).

24. R.G. Buchheit, Jr., J.P. Moran and G.E. Stoner, Corrosion, Vol. 46, No.8, pp. 610-617 (1990).

25. B.W. Likda and D.O. Sprowls, in Localized Corrosion - Cause of Metal Failure, STP 516, ASTM, Philadelphia, PA, pp. 120-144 (1972).

26. D.J. Duquette, in Environment-Induced Cracking of Metals, R.P. Gangloff and M.B. Ives, eds., NACE, Houston, TX, pp. 45-53 (1990).

27. R.P. Gangloff, in Environment-Induced Cracking of Metals, R.P. Gangloff and M.B. Ives, eds., NACE, Houston, TX, pp. 55-109 (1990).

28. M. Muller, Metall. Trans. A, Vol. 13A, pp. 649-655 (1982).

29. P.W. Tan, "The Boundary Force Method for Stress Analysis of Arbitrary Shaped Plates with Notches and Cracks", Ph.D Dissertation, George Washington University, Washington, DC (1986).

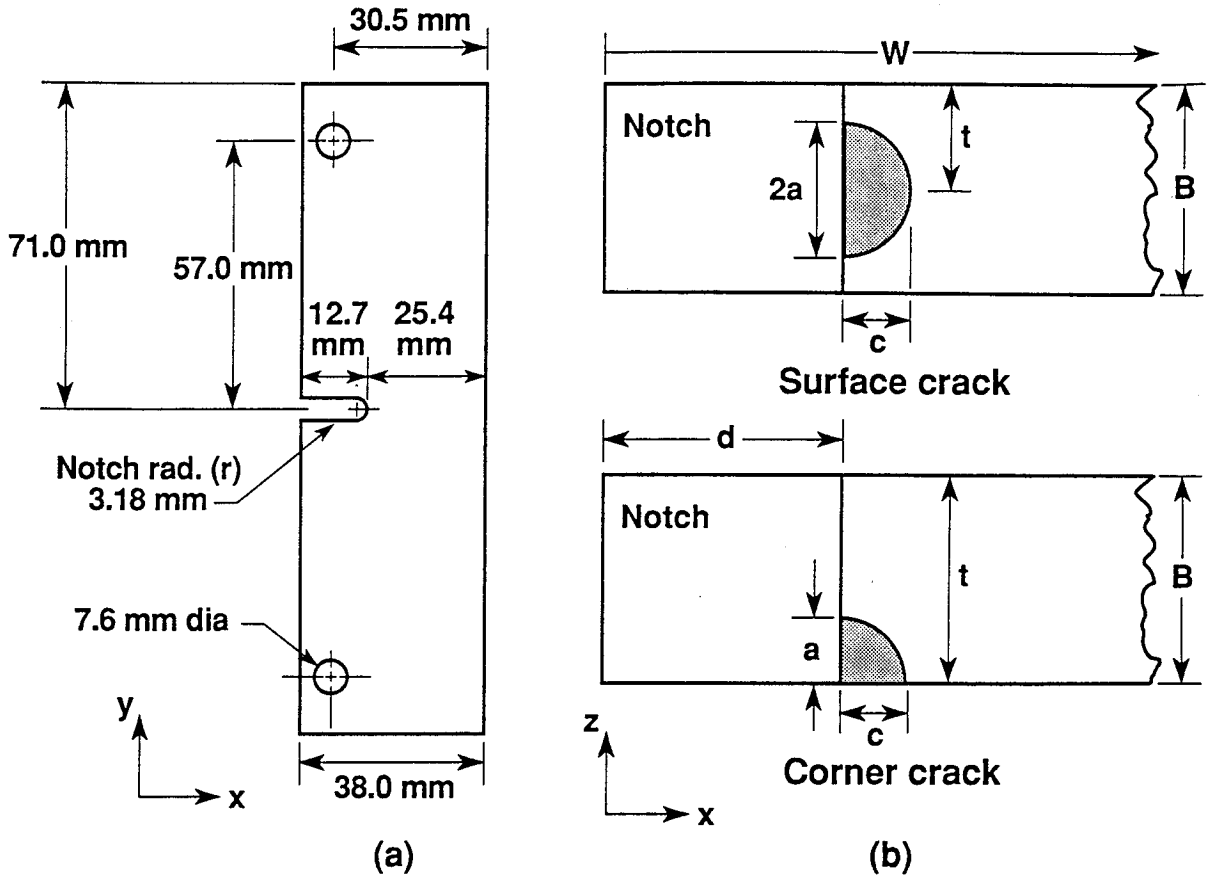

Figure 1. A schematic of, (a) the blunt notch extended compact tension specimen and (b) the surface and corner crack geometry.

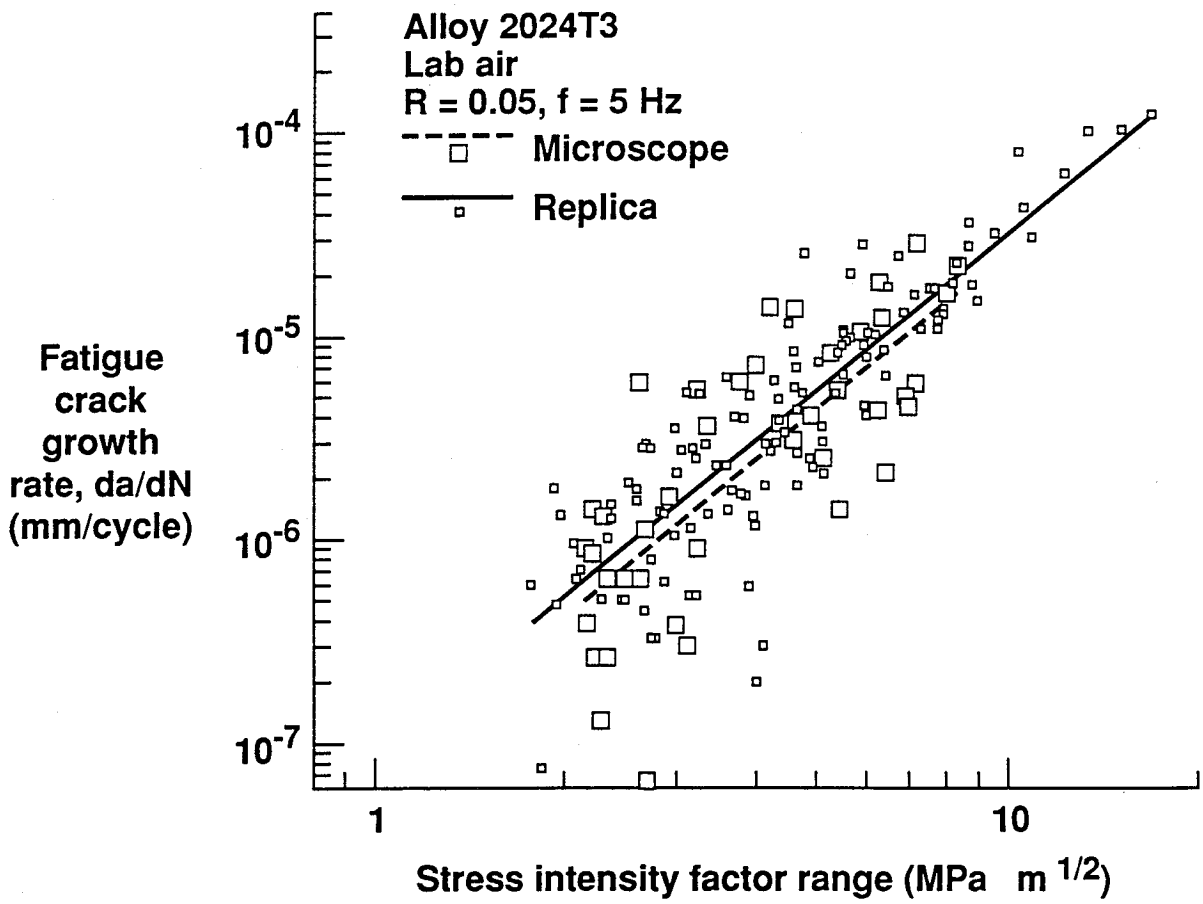

Figure 2. A comparison of laboratory air small crack growth rates using a long focal length microscope compared to the replica method.

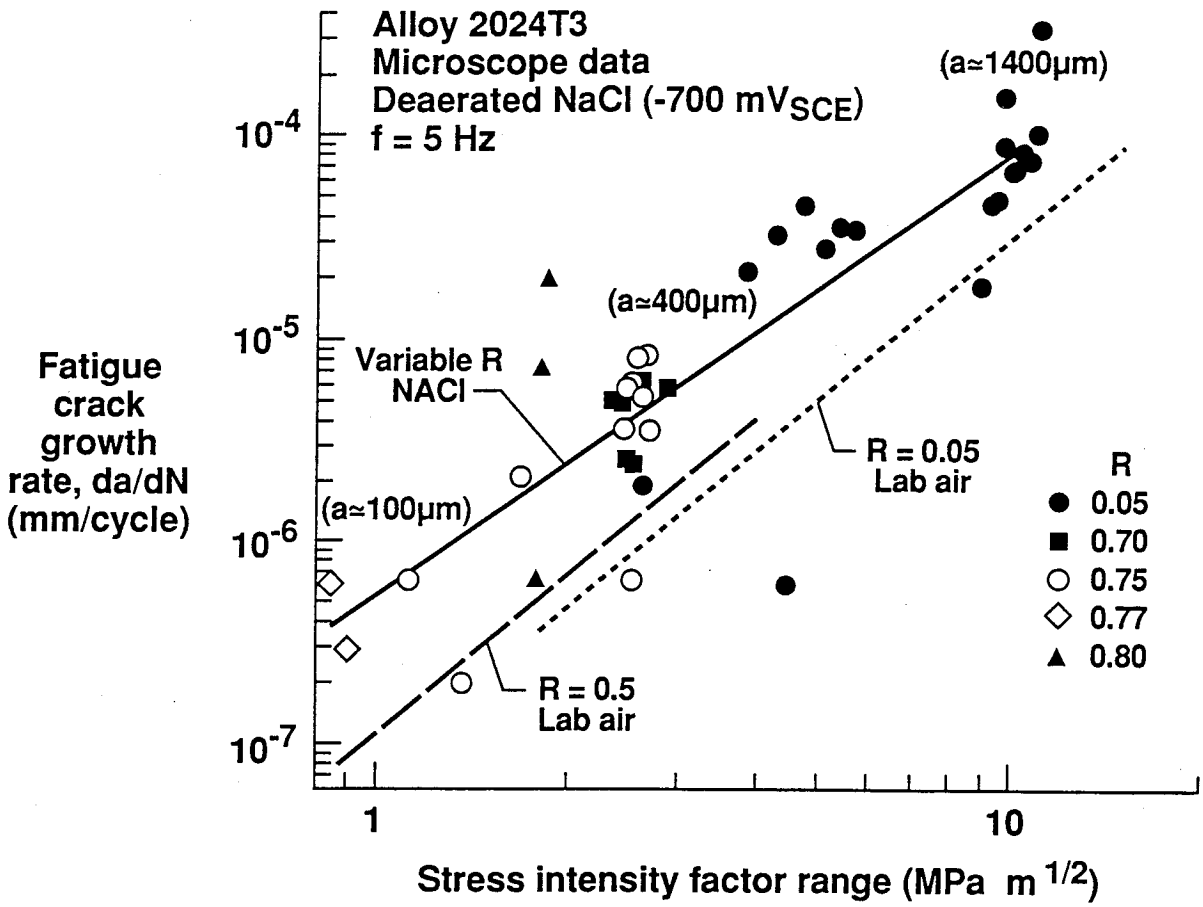

Figure 3. A comparison of small crack da/dN at variable R in salt water and constant R in laboratory air. The dashed lines are power law fits of small crack growth data; low R (0.05) from Figure 2 and high R (0.5) from Newman et.al.[18]. The approximate size of small cracks (100 μm $\leq$ a $\leq$ 1400 μm) is noted for the microscope based data; here, crack size increases with increased applied ΔK.

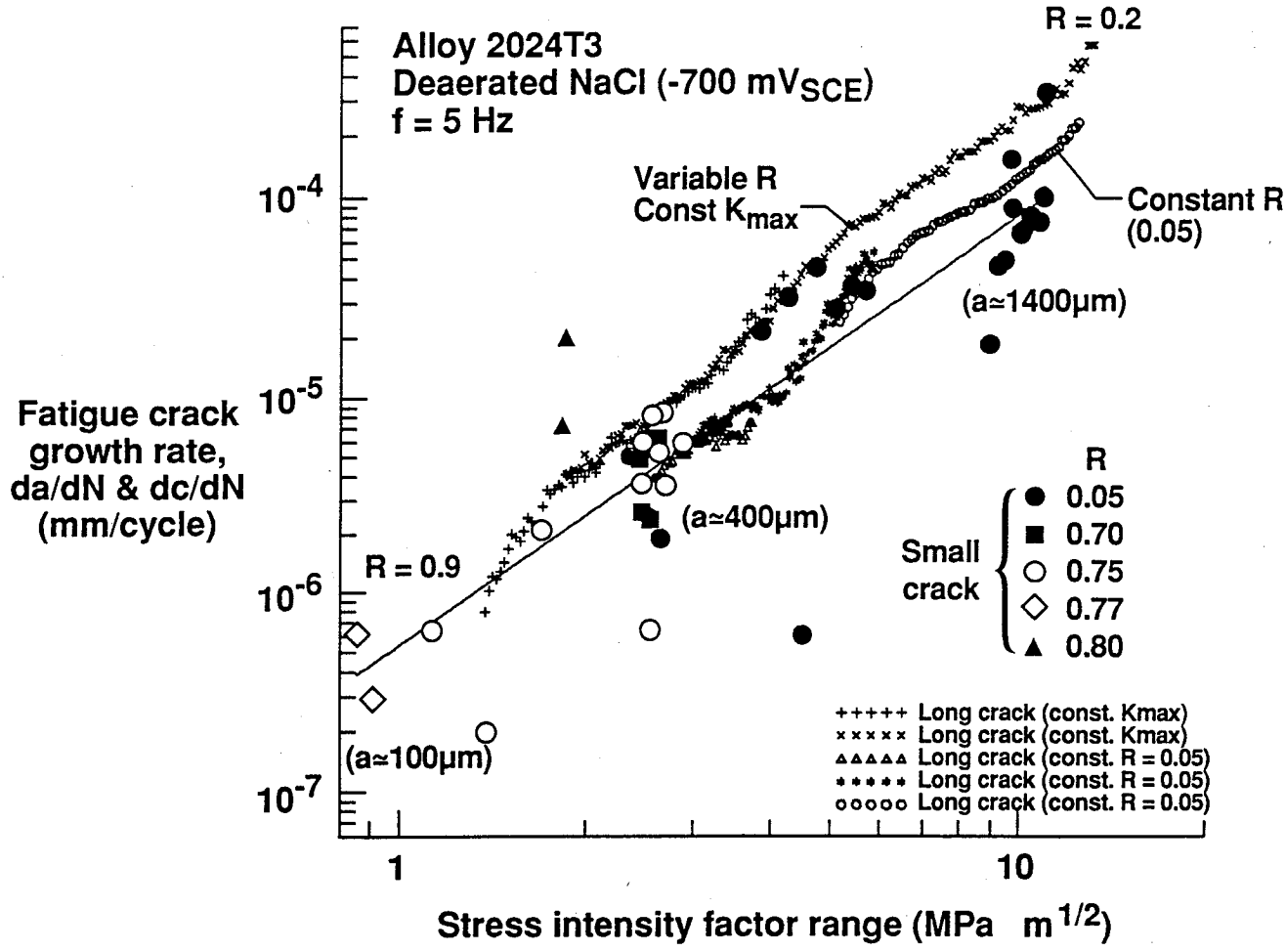

Figure 4. The corrosion fatigue crack growth characteristics of small cracks (100 μm to 1400 μm) and long cracks (14 mm to 28 mm) exposed to salt water environment. The approximate size of small cracks (100 μm $\leq$ a $\leq$ 1400 μm) is noted for the microscope based data; here, crack size increases with increased applied ΔK.

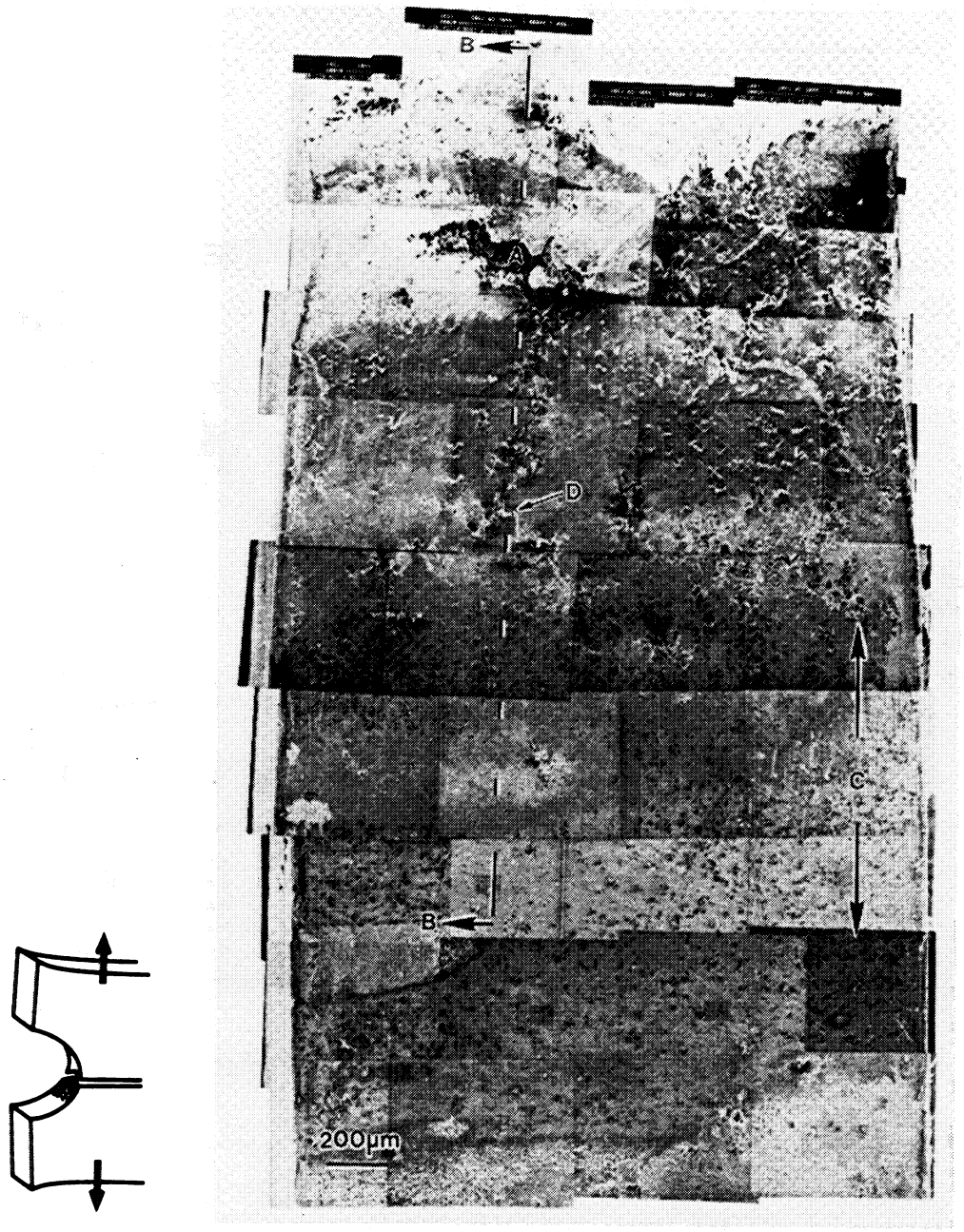

Figure 5. A montage of micrographs showing the blunt notch root surface of a corrosion fatigue specimen exposed to 1% NaCl (-700 mV_{SCE}), shaded region shown in insert.

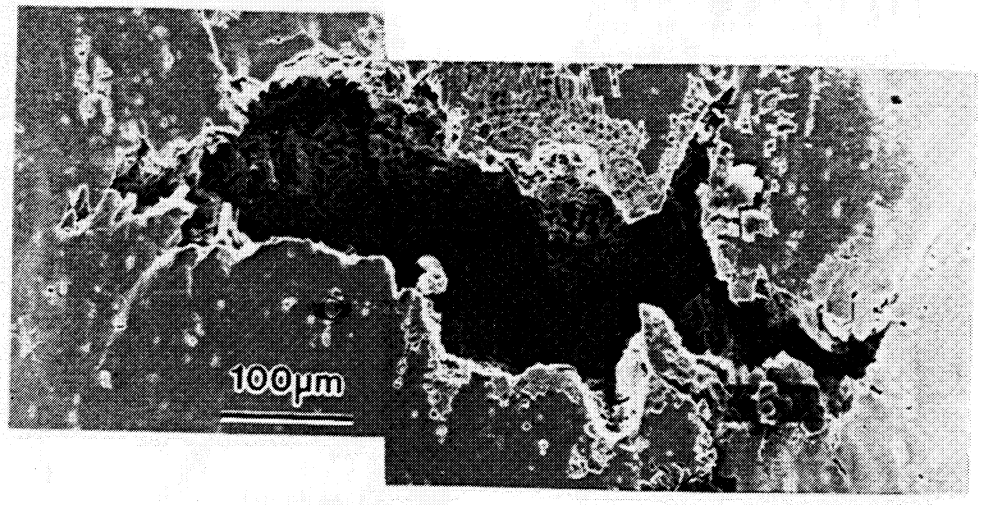

Figure 6. Micrograph showing a large intergranular crack, region A in Figure 5, in the high stress region of the blunt notch.

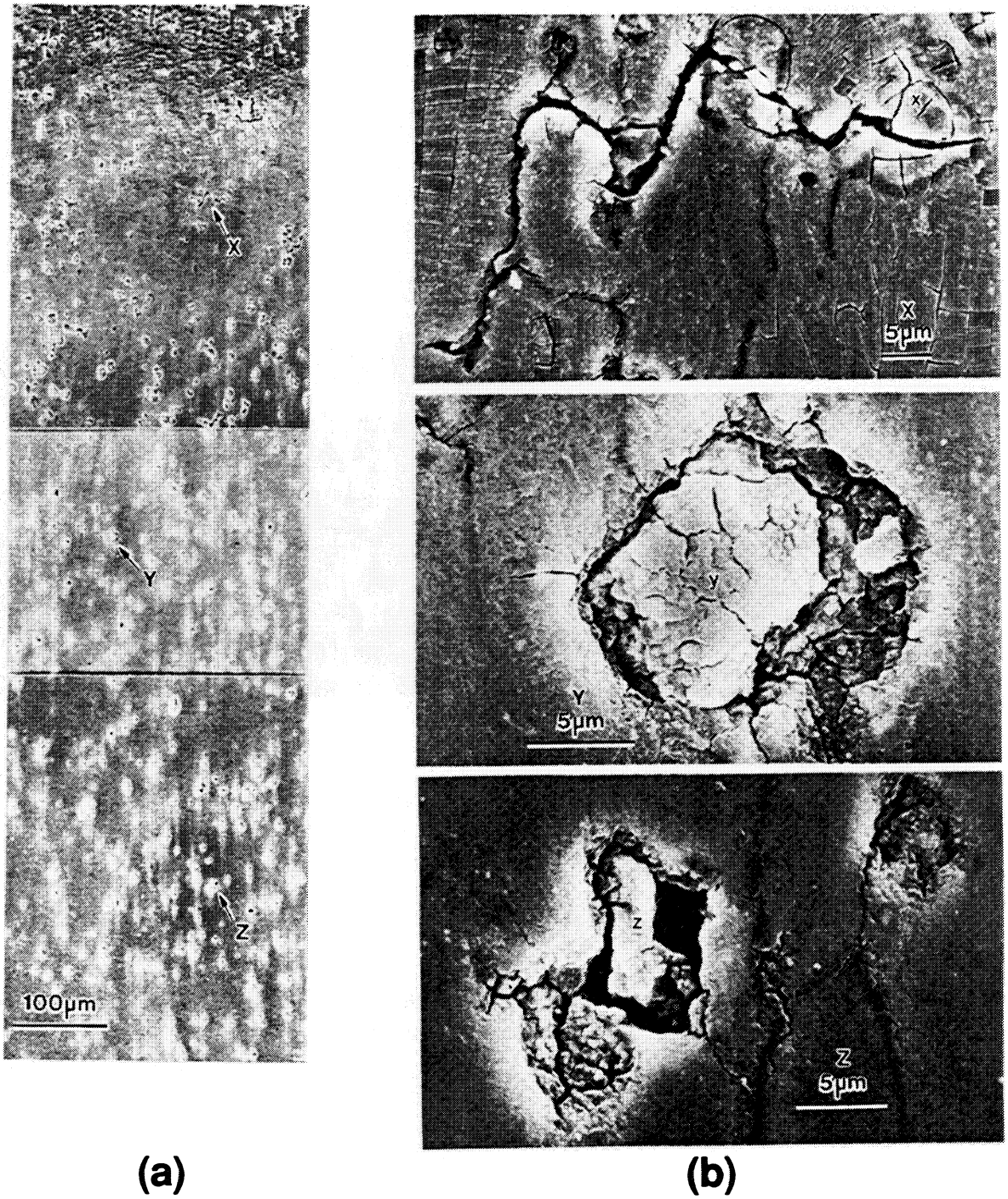

Figure 7. Micrograph showing, (a) the general area of pitting and stress assisted cracking in the low stress region of the notch, region C marked by arrows in Figure 5. (b) High magnification micrographs of regions X, Y and Z marked by arrows in (a).

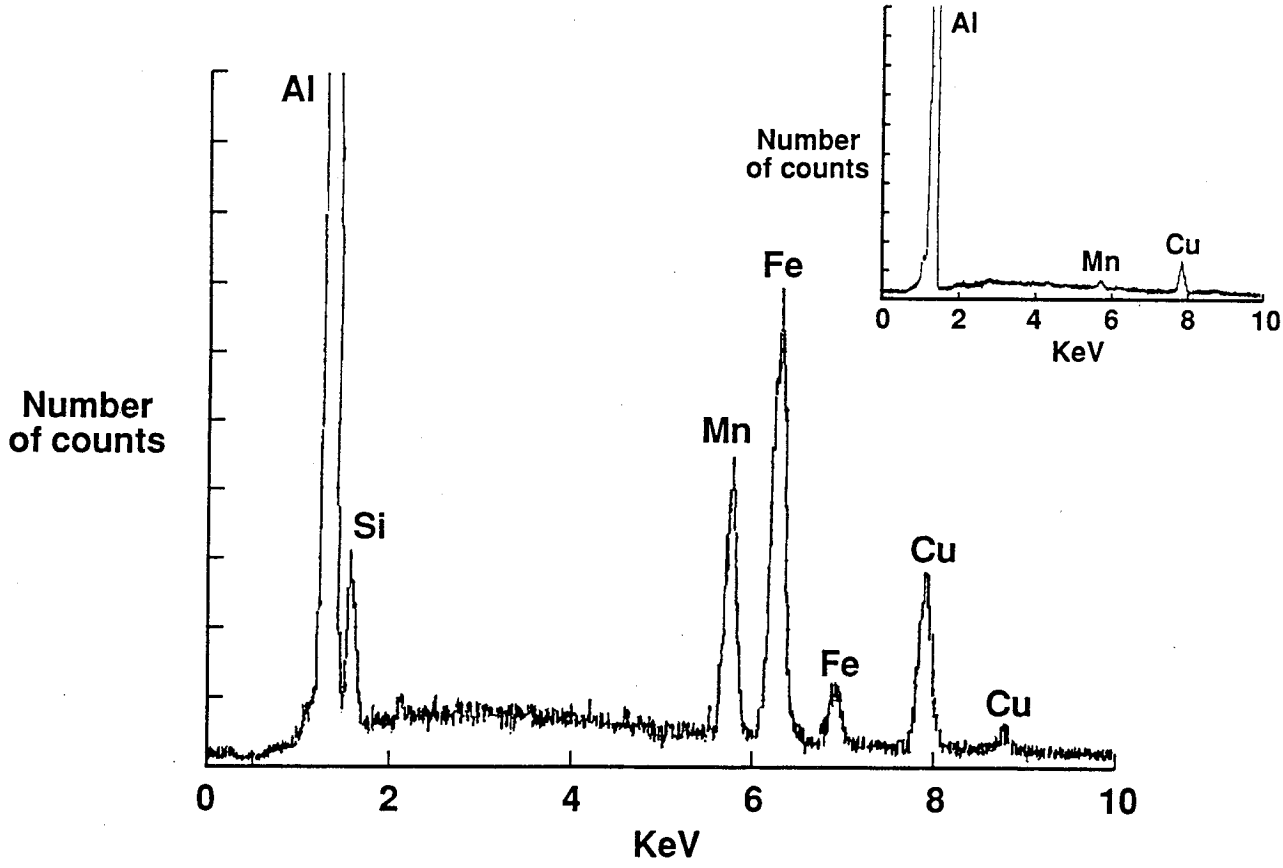

Figure 8. Emission dispersive X-ray analysis of a typical pitted region, area Z in Figure 7, reveals an increased concentration of Fe and Si compared to EDX analysis of the matrix material (insert). Similar evidence of Fe and Si rich constituent particles was observed in regions X and Y in Figure 7.

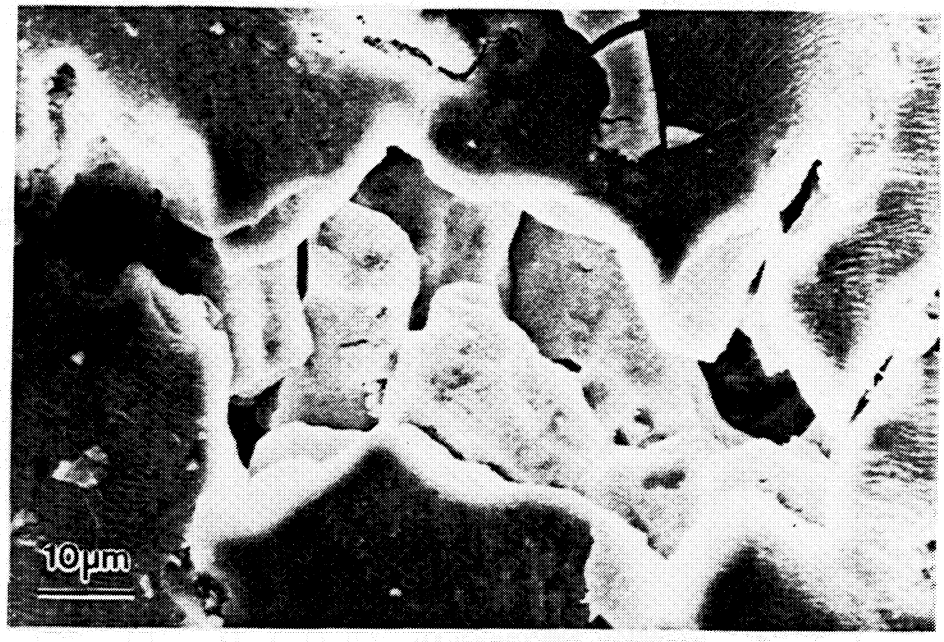

Figure 9. Micrograph showing a typical small intergranular crack in the high stress region near region A in Figure 5. Note the brittle intergranular fracture within the crack.

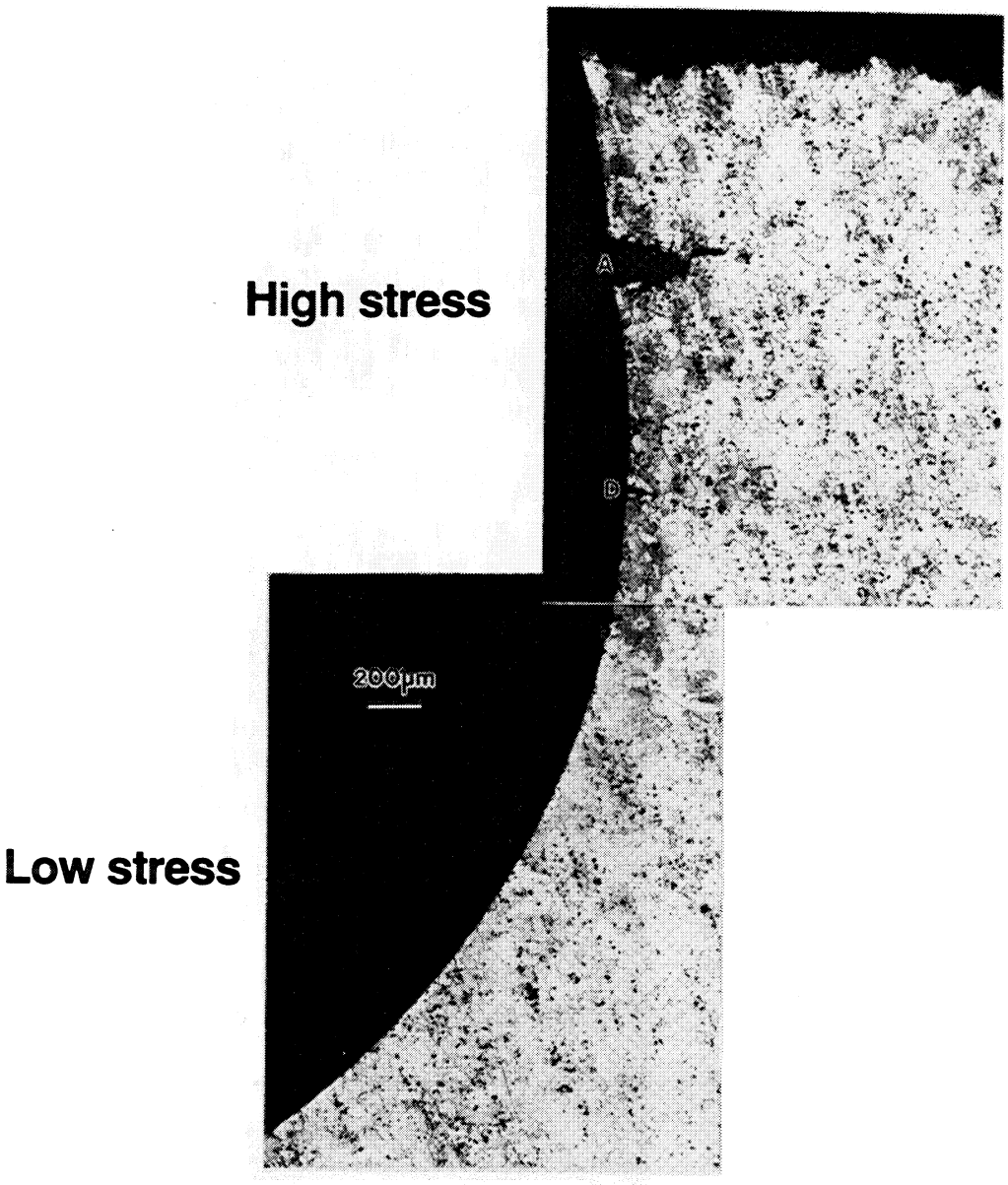

Figure 10. Metallographically prepared and etched (Keller's) section along line B-B noted in Figure 5, showing the incipient fatigue crack at A and evidence of intergranular cracking at D along the high stress region of the blunt notch surface. No evidence of intergranular cracking is shown in the low stress region.

Figure 11. Region D in Figure 10 is shown at high magnification illustrating the extent of intergranular corrosion along the high stress region of the blunt notch surface.

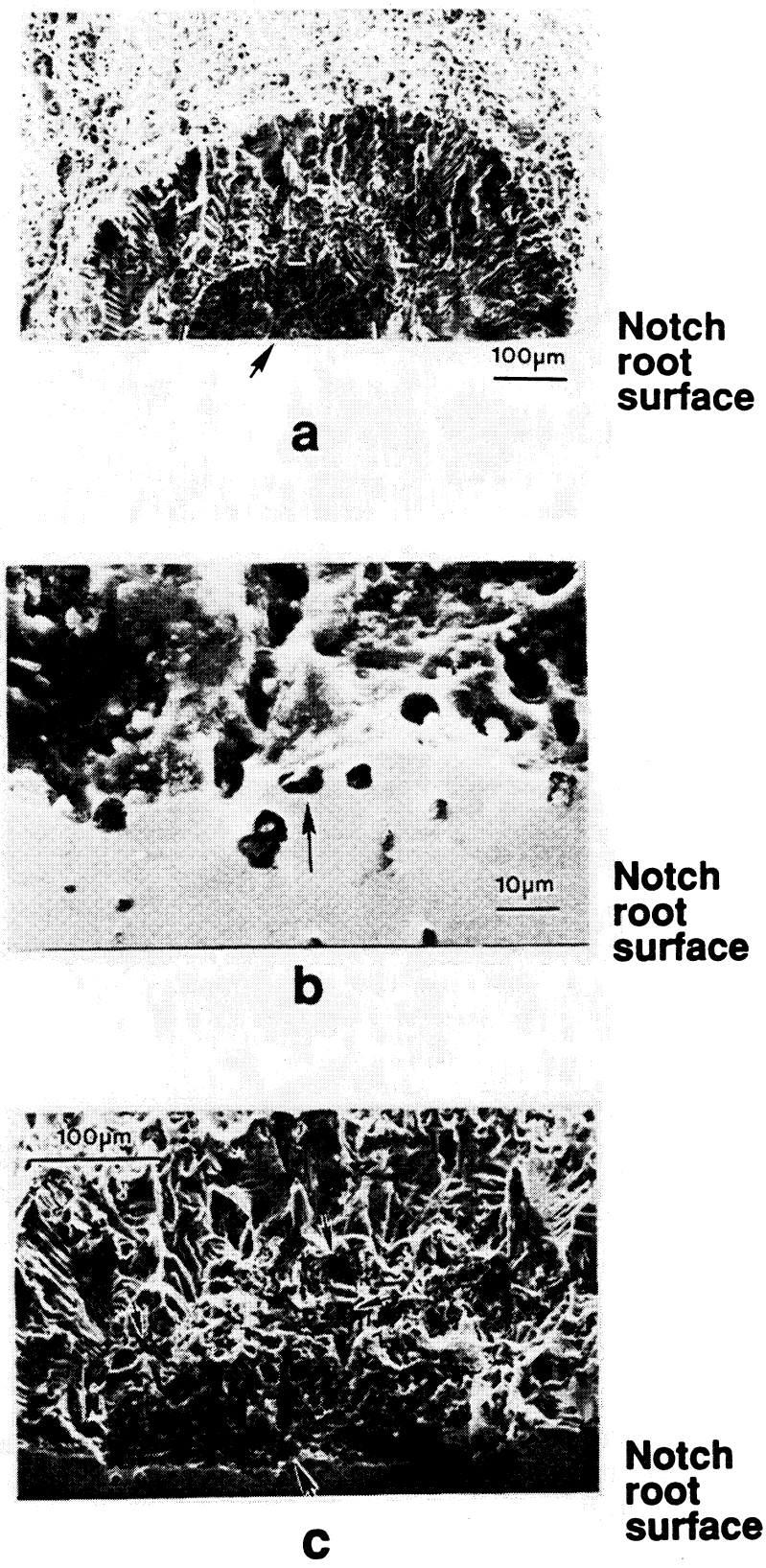

Figure 12. Fractographs showing (a) semicircular shape, crack arrest region (dashed line) and crystallographic morphology of small corrosion fatigue crack, (b) crack initiation region showing constituent particle pitting, (c) crack arrest region (shown in Figure 12a) increased corrosion due to crack arrest.

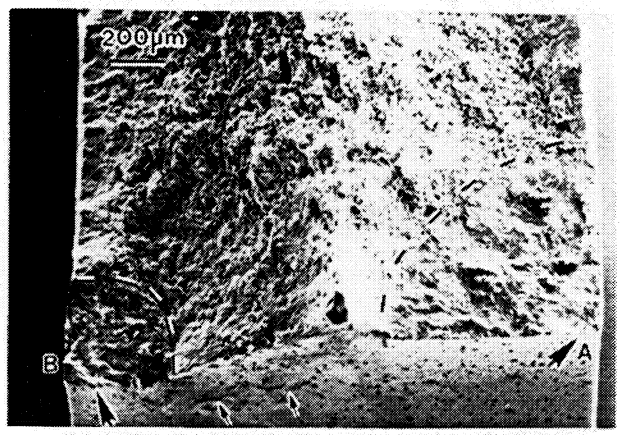

a

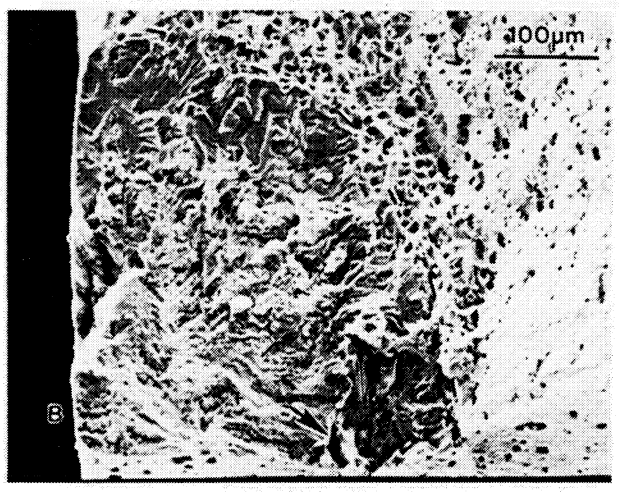

b

Figure 13. Fractographs (a) showing two corner cracks A and B and (b) micrograph showing higher magnification of corner crack B revealing crystallographic fracture morphology.

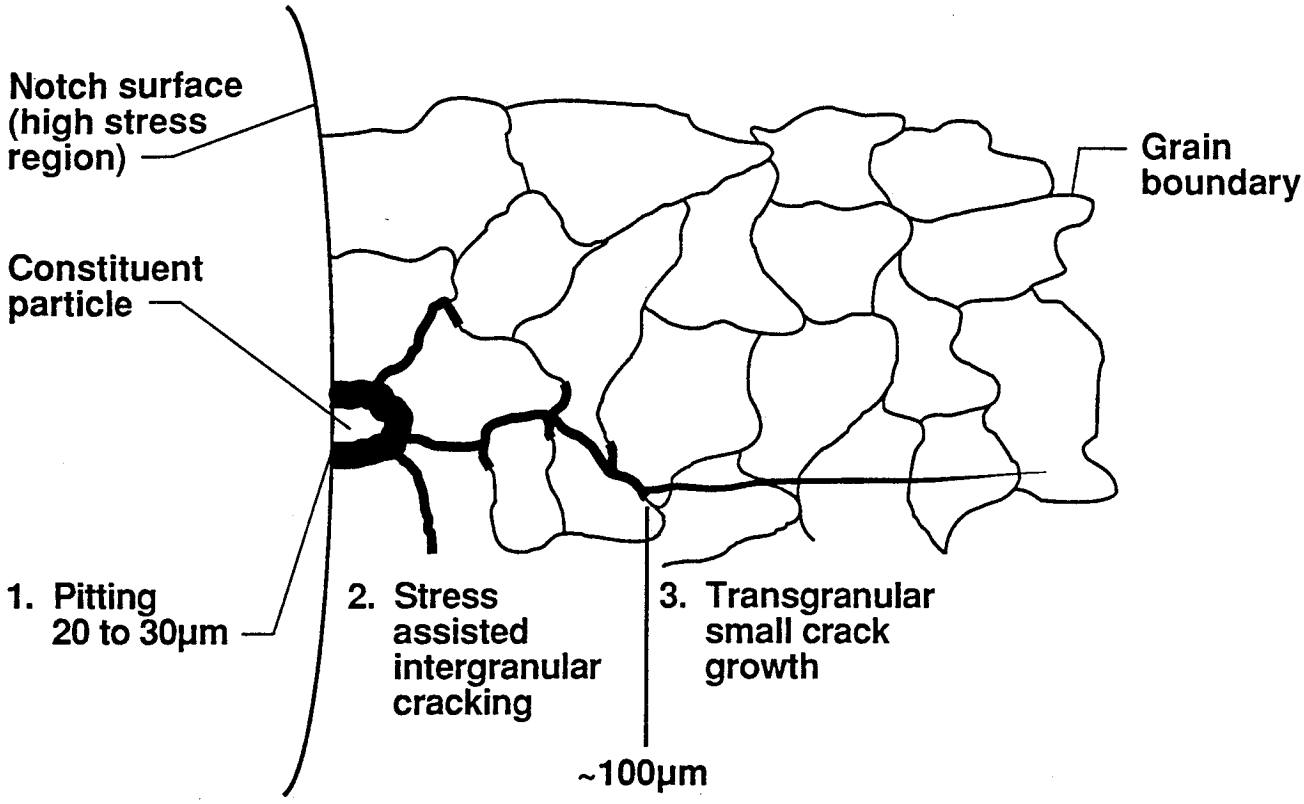

Figure 14. A schematic of the notch root radius depicting the early stages of corrosion fatigue cracking in alloy 2024. Characterized are three distinct processes: 1. constituent particle pitting, 2. intergranular microcracking and 3. transgranular small crack growth.

REPORT DOCUMENTATION PAGE

Form Approved
OMB No. 0704-0188

1. AGENCY USE ONLY (Leave blank)	2. REPORT DATE	3. REPORT TYPE AND DATES COVERED
	April 1993	Technical Memorandum

4. TITLE AND SUBTITLE

The Growth of Small Corrosion Fatigue Cracks in Alloy 2024

5. FUNDING NUMBERS

WU 538--02-10-01

6. AUTHOR(S)

R.S. Piascik and S. A. Willard

7. PERFORMING ORGANIZATION NAME(S) AND ADDRESS(ES)

NASA Langley Research Center
Hampton, VA 23681-0001

8. PERFORMING ORGANIZATION REPORT NUMBER

9. SPONSORING/MONITORING AGENCY NAME(S) AND ADDRESS(ES)

National Aeronautics and Space Administration
Washington, DC 20546

10. SPONSORING/MONITORING AGENCY REPORT NUMBER

NASA TM-107755

11. SUPPLEMENTARY NOTES

Piascik: Langley Research Center, Hampton, VA; Willard: Lockheed Engineering & Sciences Company, Hampton, VA.

12a. DISTRIBUTION/AVAILABILITY STATEMENT

Unclassified - Unlimited

Subject Category - 39

12b. DISTRIBUTION CODE

13. ABSTRACT *(Maximum 200 words)*

The corrosion fatigue crack growth characteristics of small surface and corner cracks in aluminum alloy 2024 is established. The damaging effect of salt water on the early stages of small crack growth is characterized by: 1. crack initiation at constituent particle pits, 2. intergranular microcracking for a ≤ 100 μm, and 3. transgranular small crack growth for a ≤ 100 μm. In aqueous 1% NaCl and at a constant anodic potential of -700 mV_{SCE}, small cracks exhibit a factor of three increase in fatigue crack growth rates compared to laboratory air. Small cracks exhibit accelerated corrosion fatigue crack growth rates at low levels of ΔK (<1 MPa$\sqrt{m}$) below long crack ΔK_{th}. When exposed to Paris regime levels of crack tip stress intensity, small corrosion fatigue cracks exhibit growth rates similar to that observed for long cracks. Results suggest that crack closure effects influence the corrosion fatigue crack growth rates of small cracks ($a \leq 100$ μm). This is evidenced by similar small and long crack growth behavior at various levels of R. Contrary to the corrosion fatigue characteristics of small cracks in high strength steels, no pronounced chemical crack length effect is observed for alloy 2024 exposed to salt water.

14. SUBJECT TERMS

Fatigue; Small crack; Corrosion fatigue
Crack growth; Alloy 2024

15. NUMBER OF PAGES
30

16. PRICE CODE
A03

17. SECURITY CLASSIFICATION OF REPORT	18. SECURITY CLASSIFICATION OF THIS PAGE	19. SECURITY CLASSIFICATION OF ABSTRACT	20. LIMITATION OF ABSTRACT
Unclassified	Unclassified		